Implications of X-ray beam profiles on qualitative and quantitative synchrotron micro-focus X-ray fluorescence microscopy

Alexander P. Morrell,[a] J. Frederick W. Mosselmans,[b] Kalotina Geraki,[b] Konstantin Ignatyev,[b] Hiram Castillo-Michel,[c] Peter Monksfield,[d] Adrian T. Warfield,[d,e] Maria Febbraio,[f] Helen M. Roberts,[f] Owen Addison[g,f]* and Richard A. Martin[a]*

[a]Aston Institute of Materials Research, School of Engineering, University of Aston, Birmingham B4 7ET, UK, [b]Diamond Light Source, Harwell Science and Innovation Campus, Didcot, Oxon OX11 0DE, UK, [c]European Synchrotron Radiation Facility (ESRF), 38043 Grenoble Cedex 9, France, [d]University Hospitals Birmingham, NHS Foundation Trust, Edgbaston, Birmingham B15 2TH, UK, [e]College of Medical and Dental Sciences, University of Birmingham, Edgbaston, Birmingham B15 2TT, UK, [f]School of Medicine and Dentistry, University of Alberta, Edmonton, Alberta, Canada T6G 1C9, and [g]Biomaterials Unit, School of Dentistry, University of Birmingham, Edgbaston, Birmingham B15 2TT, UK.
*Correspondence e-mail: oaddison@ualberta.ca, r.a.martin@aston.ac.uk

Synchrotron radiation X-ray fluorescence microscopy is frequently used to investigate the spatial distribution of elements within a wide range of samples. Interrogation of heterogeneous samples that contain large concentration ranges has the potential to produce image artefacts due to the profile of the X-ray beam. The presence of these artefacts and the distribution of flux within the beam profile can significantly affect qualitative and quantitative analyses. Two distinct correction methods have been generated by referencing the beam profile itself or by employing an adaptive-thresholding procedure. Both methods significantly improve qualitative imaging by removing the artefacts without compromising the low-intensity features. The beam-profile correction method improves quantitative results but requires accurate two-dimensional characterization of the X-ray beam profile.

1. Introduction

Synchrotron radiation X-ray fluorescence (SR-XRF) microscopy has become a routine technique for identifying the composition and distribution of elements in a range of sample types with high sensitivity (Jensen *et al.*, 2012; Paunesku *et al.*, 2006). The ability to focus X-rays into micrometre- and submicrometre-sized beams has allowed two-dimensional discrimination of endogenous and exogenous elements in biological substrates (Addison *et al.*, 2012). However, when investigating samples containing heterogeneously distributed elements of interest with large concentration ranges, the profile of the X-ray beam may severely affect qualitative and quantitative measurements by creating measurement artefacts.

A key assumption of quantitative XRF is that the photons within the X-ray beam are uniformly distributed in a circular or square profile (Bewer, 2015; Kanngiesser, 2003). Such uniform profiles ensures equal sampling within the beam and across the sample surface. In reality, it is difficult to produce a perfectly uniform beam shape, as synchrotron radiation is inherently structured as a result of the nature of the electron source (Bewer, 2015). A micro- or nano-X-ray beam is typically focused by a mirror system or zone plates. Zone plates
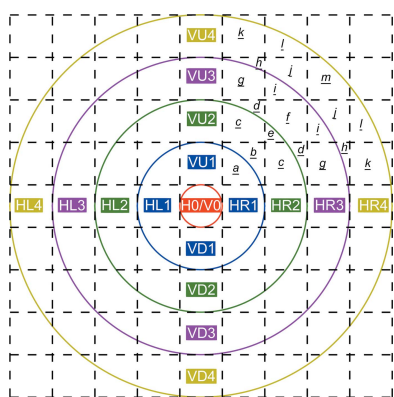
provide superior resolution, enabling a spot size well below 1 µm to be achieved; however, they sacrifice X-ray flux and are limited in the energy range that can be focused (Yun *et al.*, 1999). A popular choice for a mirror system is the Kirkpatrick–Baez (KB) system, which consists of two mirrors focusing horizontally and vertically; the system enables a larger flux and broader energy range to be achieved (Eng *et al.*, 1998). The focused X-ray beam does not typically have a square-function profile where the intensity is binary. Instead it has an intensity profile which is usually Gaussian and the size of the beam is taken as the full width at half-maximum (FWHM) of this profile. In addition, the focusing optics may introduce elements of non-uniformity to this profile, skewing the Gaussian or introducing asymmetric features (Mori *et al.*, 2002; Liu *et al.*, 2005). Therefore ∼70% of the flux is within the FWHM and hence the calculated beam size; this results in a substantial proportion of the total flux exciting adjacent pixels if a step size similar to the FWHM is adopted. This has no effect on perfectly homogeneous samples as the peripheral excitation is occurring on pixels with identical concentrations. Therefore, the photo-electron interactions lost within the central pixel, caused by reduction in flux, are gained from exciting adjacent pixels. Interrogation of a homogeneous material yields the same results irrespective of the beam profile; however, this is not the case when interrogating heterogeneous features. When the beam centre is adjacent to features with large intensities, the tails of the beam cause peripheral excitation which results in the production of image artefacts. The magnitudes of these artefacts are dependent on the size of the feature in relation to the width of the beam. Features with high intensities that are similar in size to the beam produce the most noticeable artefacts, which significantly affect the qualitative and quantitative results. In addition, the profile has a direct effect on the quantitative measurement as it is calculated based on the assumption that 100% of the flux is within the central pixel. If only 70% of the flux is within this region it is possible that the concentration of each pixel within the map is underestimated by up to 30% if the neighbouring pixels contain no signal, or overestimated depending on the elemental concentration in the surrounding pixels.

To the best of our knowledge, for the first time image artefacts in SR-XRF microscopy are discussed. Two distinct correction methods are described.

2. Materials and methods

2.1. Sample preparation

Ex vivo tissue sections of peri-implant inflamed skin and/or subcutaneous soft tissue were obtained from consenting patients undergoing revision surgery, associated with a commercially pure Ti bone-anchored hearing implant, at the University Hospital Birmingham NHS Foundation Trust. Ethical approval was provided by the UK National Research Ethics Service (approval 15/NW/0079). Tissue blocks were paraffin embedded, sectioned at 3 µm and mounted onto ultra-pure fused silica microscope slides (<10 p.p.b. Ti; Spectrosil 2000, Heraeus Quarzglas GmbH & Co., Hanau, Germany). Similarly prepared sections (formalin-fixed paraffin-embedded) of murine spleen containing Ti were collected from animals, [(12–16 weeks of age) male C57BL/6 J mice (Jackson Laboratories, Bar Harbour, ME, USA)] and exposed to a sterile intraperitoneal inflammation model [thioglycollate and TiO_2 nanoparticles (<50 nm)]. Mice were injected into the intraperitoneal cavity with saline containing 4% thiolglycollate (Sigma, 70157, Oakville, ON, Canada) and 10 p.p.m. suspended TiO_2 (Sigma, 637253) nanoparticles, after which the mice were left for 8 h before sacrificing. Animal studies were approved by the University of Alberta Health Sciences Animal Welfare Committee. Spleens were extracted from the mice and immediately fixed in neutral buffered formalin (10%; Sigma, HT501128, Oakville, ON, Canada), embedded in paraffin and 3 µm sections were mounted on 200 nm silicon nitride membranes (NX5300D, Norcada, Edmonton, Canada).

2.2. XRF measurements

XRF was undertaken on *ex vivo* peri-implant tissue sections at the microfocus beamline I18, Diamond Light Source (DLS) (Mosselmans *et al.*, 2009). An incident monochromatic X-ray beam of 5.7 keV was selected using a Si(111) double-crystal monochromator and focused to a beam size of ∼3 µm × 3 µm by a KB mirror system. An irradiation time of 100 ms per point was utilized and the fluorescence signal was recorded using two four-element Vortex Si drift detectors positioned at 45° to the sample (90° to the incident X-rays). An on-the-fly acquisition method was adopted with a step size of 3 µm vertically and horizontally. Data were collected using a calibrated diode and thin-film reference material (AXO, Dresden, Germany) for a flux measurement and to calculate geometric parameters for quantification. Data were batch fitted quantitatively using *PyMCA* (version 5.1.3; Solé *et al.*, 2007) which uses a fundamental-parameters algorithm, outputting the data as a mass fraction (Rousseau & Boivin, 1998; Thomsen, 2007).

Murine tissues were XRF mapped at the X-ray microscopy beamline ID21, European Synchrotron Radiation Facility (ESRF) (Salomé *et al.*, 2013). Similarly to the measurements at DLS, a fixed-exit double Si(111) crystal monochromator was used to generate an incident energy of 5.1 keV, and was focused down to a beam size of ∼1 µm × 1 µm by a KB mirror system. A 100 ms irradiation time was used and the fluorescence signal was detected by an XFLASH 5100 Si drift detector. The measurements were also acquired on-the-fly in a raster pattern with steps of 0.5 µm vertically and horizontally. The data were analysed in *PyMCA*, qualitatively outputting the data in counts.

3. Results and discussion

3.1. Beam-profile artefacts

One map from each tissue type was chosen to highlight the presence of the beam-profile artefacts. Figs. 1(*a*) and 2(*a*) show
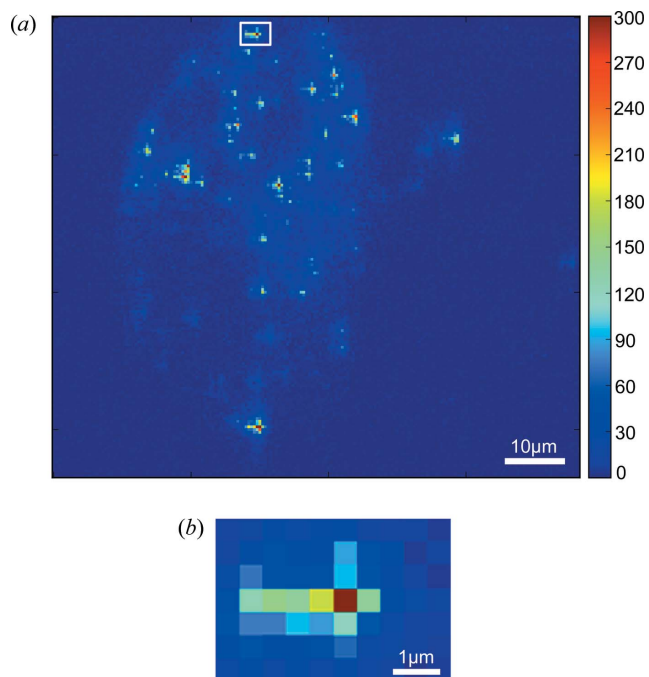
Figure 1
(*a*) Ti XRF map on a murine spleen recorded at ID21, ESRF (experiment number: L2713). The scale bar represents the number of counts. (*b*) Expanded image of the artefact taken from the region highlighted by the inset white box. Fluorescence intensity is represented on a linear scale in arbitrary units.
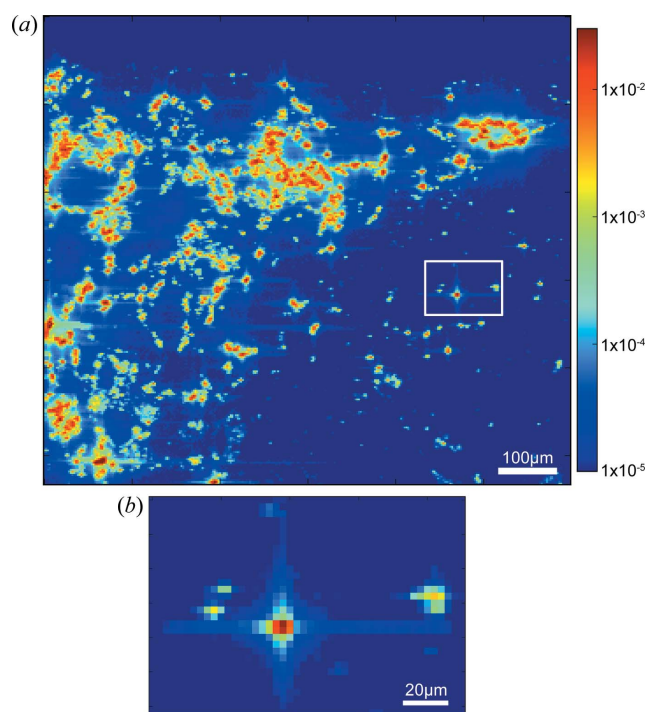
Ti XRF maps taken from ID21 and I18, respectively, Figs. 1(*b*) and 2(*b*) are sections from within the corresponding maps to emphasize the presence of these artefacts.

These artefacts are caused by the beam excitation of adjacent areas and in both cases are larger horizontally. The artefacts contain a cross-like pattern, extended vertically and horizontally, when observed on an isolated feature. When a cluster of features are within close proximity, the artefact tails may merge together giving an elevated signal surrounding high-intensity particle groups. Within the ID21 data in Fig. 1, the artefacts are asymmetric with a larger contribution to the left-hand side; this is explained when looking at the horizontal wire scan in Fig. 3. It should be noted that if there are features within the map that are smaller than the pixel size, this may introduce further complexity as the data are measured on-the-fly. This may affect the size of measured features as sub-pixel-sized particles at the periphery of pixels may contribute to the signal in more than one pixel; however the calculated concentration will not be affected. To rectify this, a step measurement can be utilized, although this is impractical for larger maps because of the significantly increasing measurement times. A higher-resolution X-ray beam can also be used but is instrument-dependent and will sacrifice the area of the sample being interrogated.
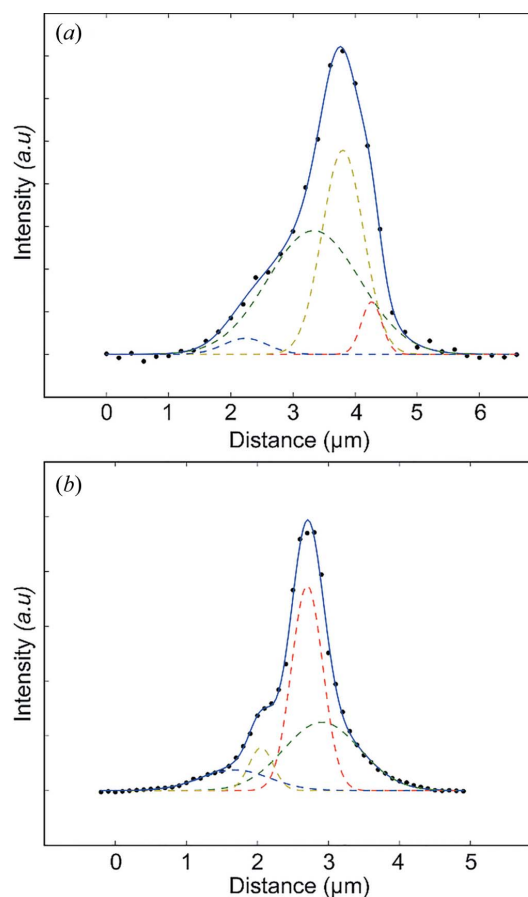

Figure 2
(*a*) Ti XRF map on *ex vivo* human soft-tissue taken from the area adjacent to the bone-anchored implant, recorded at I18, DLS (experiment number: nt-16838). The coloured bar represents the mass fraction. (*b*) Expanded image of the artefact from the region highlighted by the inset white box.

Figure 3
Wire scans from ID21. Horizontal (*a*) and vertical (*b*) wire scans (black dots) complete with four Gaussian profiles fitted (dashed lines), the sum of the fit is shown as a solid blue line. A step size of 150 nm was used and the intensity was measured in a transmission geometry.

research papers

3.2. Wire-scan measurements

Horizontal and vertical wire scans were recorded at ID21 to calculate the beam size. These scans are shown in Fig. 3 complete with a multi-Gaussian fit.

The resultant fit was segmented into areas representing the x and y step size used for the XRF maps (0.5 μm), and normalized flux intensities were calculated for each section by integrating the sum of the Gaussian equations. Fig. 4 graphically highlights the segmentation with corresponding normalized contribution values.

It is evident from Fig. 4 that a large proportion of the incident photons are present outside of the central region (red) as far as 2.5 μm away from the maximum, resulting in the excitation of peripheral areas. In this particular case, the maps were oversampled by a factor of two in order to increase the spatial resolution, which increases the amount of sample excited outside the nominal pixel.

In samples where highly concentrated heterogeneous elements of interest are present, the tails of the beam can excite these areas even when the beam centre is not on the feature. This peripheral excitation dominates the signal, generating a false-positive result. As a consequence, it appears that Ti is present at low concentrations in areas surrounding highly concentrated particles, which may not be the case. The presence of these artefacts severely affects the accuracy of qualitative and quantitative XRF imaging. From a qualitative perspective, the artefact may lead to inaccurate measurements of the size of the features and incorrect reasoning for the elemental distributions observed. It will significantly affect any attempts to correlate elemental distribution with underlying sample features (e.g. cellular composition of tissues) because of uncertainty in location, and/or correlation with other elements recorded simultaneously. The artefacts will cause overestimations in percentage coverages, affect average-concentration calculations and the distributed beam profile will result in inaccurate single-pixel quantification. It should be noted that the artefacts will only be present in samples that exhibit specific features. Firstly, the samples must be heterogeneously distributed, otherwise artefacts will appear evenly throughout the image and would be accounted for mathematically with the use of a reference material (assuming adequate beam stability between measurements). The samples must also have a large concentration distribution; the high-concentration features will generate the artefacts when processed, but a threshold cannot be applied to remove them as the low-concentration features within the map would be lost. A simple background subtraction or minimum threshold cannot be applied as there are many regions within the map that contain lower-intensity pixels than those where the artefacts are responsible for much of the intensity. The effect of minimum thresholding is shown in Fig. S1 of the supporting information. The low-concentration features are of equal importance to the high-intensity particles, therefore two distinct mathematical-correction methods were developed to remove the observed artefacts.
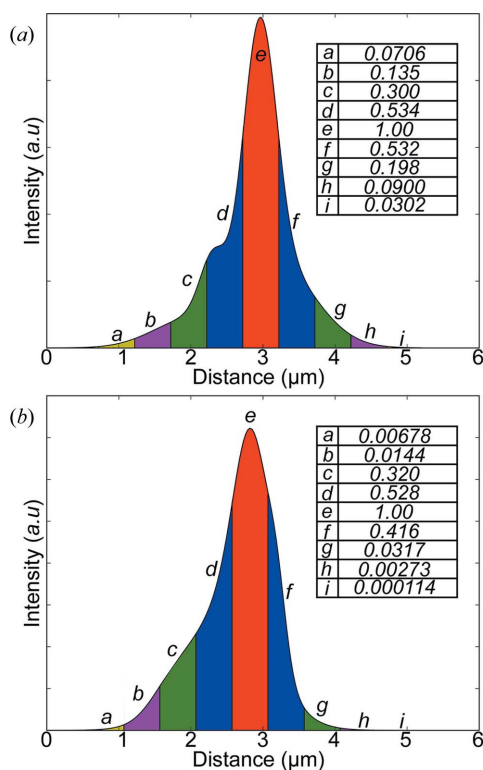
3.3. Beam-profile correction

The beam-profile correction is a form of image deconvolution, which is routinely used in a variety of microscopy methods to mitigate image artefacts (Swedlow et al., 1997; Lanteri et al., 1994), but, to the best of our knowledge, have never been applied to XRF images. Images recorded are combinations of objects present that are multiplied by a point-spread function (PSF), which is intrinsic to the measurement device. Many image-deconvolution methods require pre-existing knowledge of the PSF to reverse the image to more effectively represent the objects present (Swedlow, 2007; Shaw & Rawlins, 1991; Shaevitz & Fletcher, 2007). In this case, the beam profile can be considered as the PSF and, in theory, by accurately knowing the beam-profile contributions, the XRF images can be deconvoluted into more accurate data. As every SR-XRF beam profile contains a different X-ray distribution and varies significantly, according to the measurement objectives, the deconvolution method must be versatile to be utilized widely. Pre-existing deconvolution methods such as those found in *ImageJ* libraries may help reduce the presence of artefacts observed in XRF images (Sage et al., 2017). However they do not consider that the quantification of a single pixel is based on a calculation whereby 100% of the flux is present. As this does not hold true, an important re-normalization step is needed once an appropriate correction is undertaken; this will ensure more accurate single-pixel quantification.
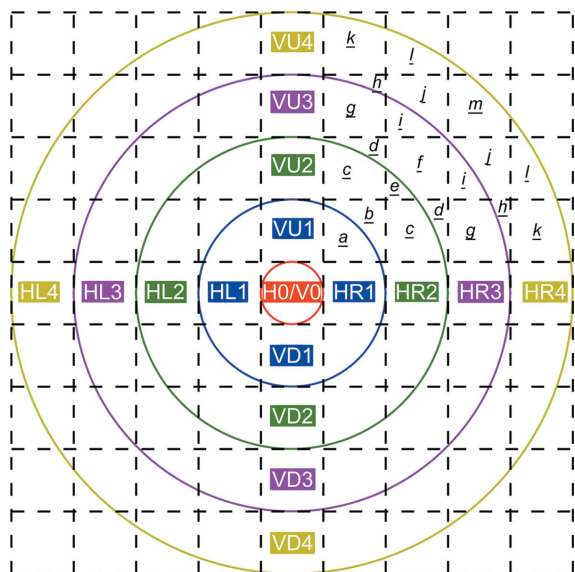

Figure 4
Fit of the horizontal and vertical segmented wire scans (500 nm). Normalized contributions are generated from integrating the fit equation and are listed (a–i).

Figure 5
Different scale factors used for each pixel in the quadrant. The scaling factors are listed in Table S1 of the supporting information.

The principle behind the correction was to use the beam profile (as recorded by the wire scans) to calculate the exact contributions of surrounding pixels (attributed to the beam tails) and correct each pixel accordingly. As the wire scans provide a horizontal and vertical profile through the centre of the beam, a two-dimensional profile was calculated geometrically. Fig. 5 displays a schematic diagram highlighting the profile of the beam. An assumption was made whereby the quadrants were calculated with a circular profile. This allowed a scaling factor to be generated for each vertical and horizontal pair, for example, the scaling factor for VU1 and HR1 is _a_ (0.532) and for VU2 and HR2 is _b_ (0.468), and are both used to evaluate the single pixel (HR1, VU1) (shown in Fig. 5). As the pixel is equidistant from both the horizontal and vertical components, an equal contribution from each is assigned. However, if a pixel is closer to the vertical components, a weighting factor is applied such that more contribution is assigned from the vertical measurements than the horizontal and _vice versa_. The factors are calculated based on the distance between the contributor (vertical or horizontal) and each quadrant pixel.

Following the calculation of the two-dimensional contribution based on the horizontal and vertical wire scans, an iterative process was applied, making corrections from the smallest value in the map to the highest. The beam-profile correction process is detailed in Fig. 6. It should be noted that an 8 pixel border around the map is not corrected as intensity values outside the map are not known. Therefore, this region is cropped from the final image.

Fig. 7 shows an XRF map of murine tissue interrogated at ID21, following processing with the beam-correction iteration. It is evident that the artefacts are greatly reduced and that the low-intensity pixels distant from high-concentration features are still present. In addition, the size and distribution of particles are now closer to their expected values, considering
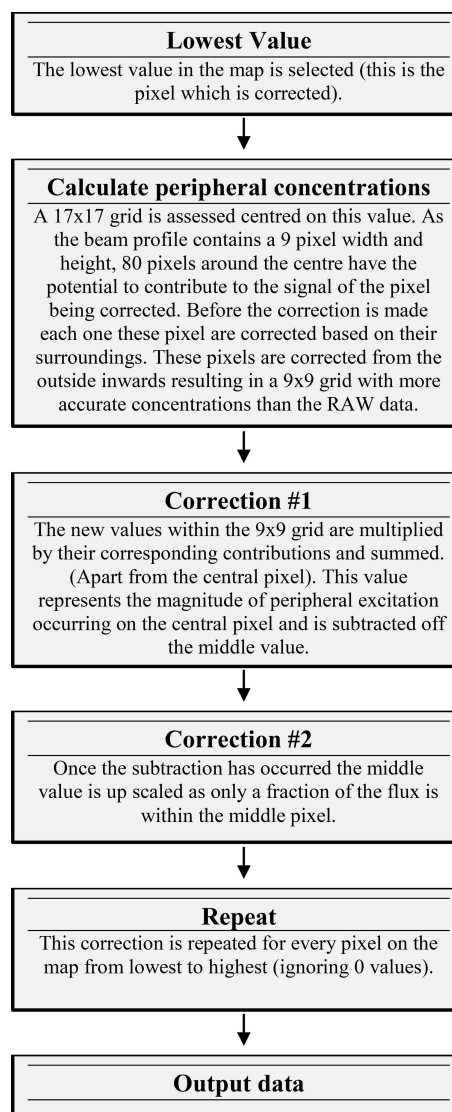

Figure 6
Flow diagram detailing the processes involved in the beam-profile correction.

the initial exposures of dispersed nanoparticles. Fig. S2 of the supporting information shows a small section of the map before and after the beam-profile correction containing a cluster of particles with their intensities displayed.

3.4. Adaptive subtraction

The beam-profile correction method relies on having a high-quality two-dimensional beam profile, which may not be available to the investigator, hence an alternative approach was developed. An adaptive-subtraction method was produced which enables a correction only using the image data; this facilitates retrospective analysis and artefact removal when the beam profile is unknown.

This correction relies upon a subtraction which is influenced by the values of surrounding pixels. Similar to the beam-profile correction method, each pixel is assessed within the map and assigned an appropriate baseline correction. During
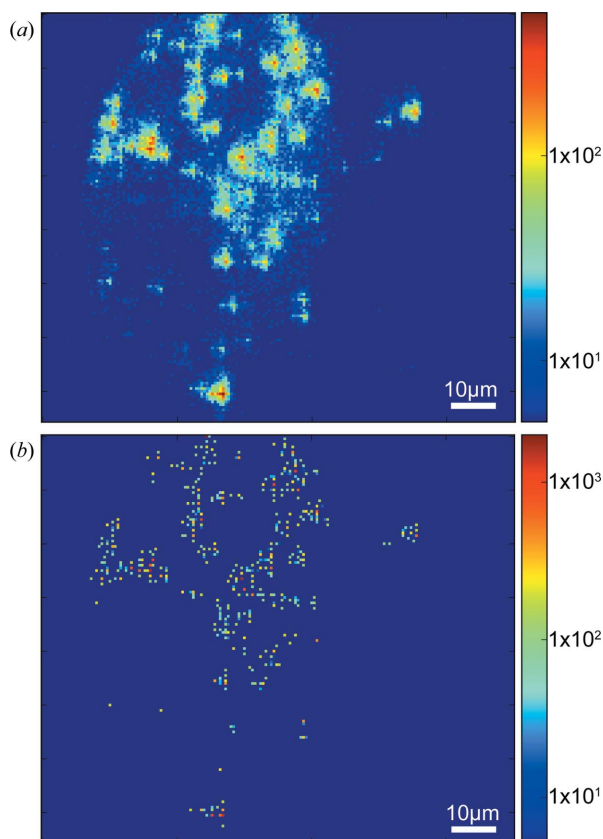
Figure 7
The result of the XRF map shown in Fig. 1 after undertaking beam-profile correction: (*a*) before correction and (*b*) after correction. The coloured bar represents counts.

the correction, horizontal and vertical profiles were assessed that contained the highest pixel value, which covered the entire width and length of the map. The profiles were subsequently fitted with cubic-spline functions. As the baseline changes unpredictably, a mathematical function is inappropriate without carefully studying each fit. Polynomial functions within datasets such as these tend to oscillate unpredictably in between background anchor points, resulting in a poor fit. A cubic spline provides a robust method for this type of baseline correction in scenarios with variable peak widths, large changes in background intensities and processes with short computational times (Yi *et al.*, 2015). An example of a single horizontal profile complete with a cubic-spline background function is shown in Fig. 8.

The background function was subtracted from the original data. As each pixel is corrected twice, horizontally and vertically, only the smallest value of the original data minus the background is used in the corrected map. The obtained corrected map is shown in Fig. 9. The image artefacts are greatly reduced following the adaptive threshold and the low-concentration pixels (highlighted earlier) are still present. The background function subtraction works on the premise that areas surrounding larger-intensity features are elevated as a result of peripheral excitation. The intensity of the function at a given area is therefore dependent on the adjacent values. A background value adjacent to a 100 p.p.m. particle compared
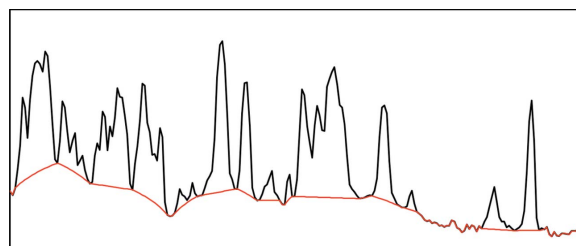

Figure 8
Horizontal profile complete with cubic-spline background function. A logarithmic scale is used on the *Y* axis to highlight subtle changes in intensity.

with a 10000 p.p.m. particle may differ by several orders of magnitude and cannot be used appropriately to correct for both intensities.

Following the adaptive threshold, the concentrations are lower than the original values as a subtraction has been applied. Pixels that are considered artefacts are reduced significantly; the magnitude of the subtraction is dependent on the concentration of the contributing Ti feature. The empty background pixels (away from any features or artefacts) are reduced by an order of 1–3% (largely contributed by noise), the pixels surrounding the wear particles decrease by <0.5% and the wear particles decrease by <0.01%. The accuracy
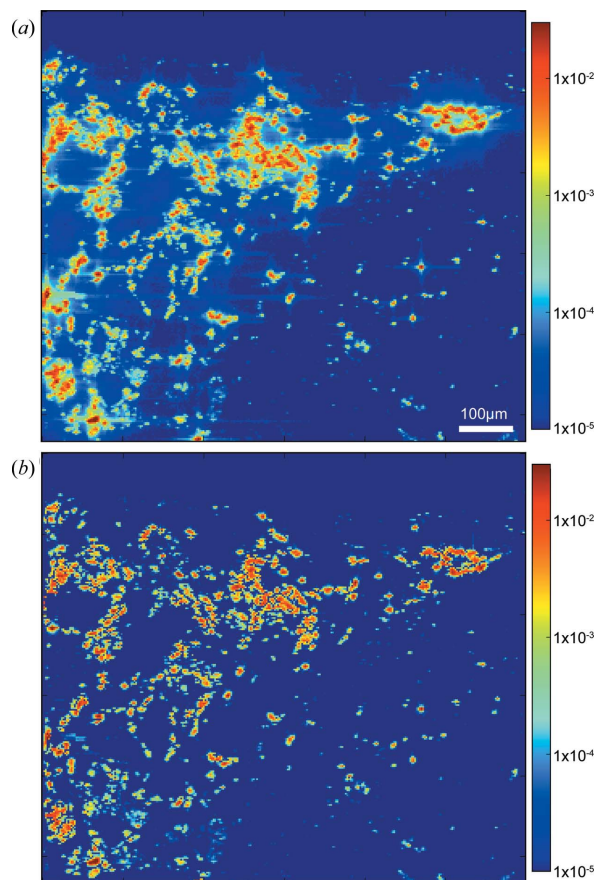

Figure 9
Ti XRF maps showing the adaptive subtraction (*a*) before the correction and (*b*) after the correction. The coloured bar represents mass fraction, displayed on a logarithmic scale.

of average concentrations and percentage coverages are improved following the correction, which can be attributed to the reduction of artefacts. The maximum concentration is reduced by <0.01%; this negligible change is within the errors of quantification. However, no subsequent re-normalization was undertaken to account for the fact that only a fraction of the flux is within the central pixel. Although this method significantly improves qualitative imaging, the beam-profile normalization is deemed far more accurate for quantitative analysis.

Both correction methods possess advantages. The beam profile correction method should yield accurate quantitative results; however, the quality of the correction relies on the beam-profile measurement. The profile generated from the wire scans is somewhat limited at its extremities, as transmission detectors are, in general, substantially less sensitive than fluorescence detectors, which are used in measuring the map. When approaching the wire with the X-ray beam, the noise associated with the transmission ion chamber limits the detection of photons at the edges of the beam. Areas at the edges of the curves in Figs. 3 and 4 may not be zero, but the transmission detector may not possess sufficient sensitivity to detect a subtle change. Therefore, this limits the correction based on the sensitivity of measuring the beam profile. In addition, the profile is generated based on the assumption that the beam is circular, hence imaging the beam with a suitably sensitive camera could obviate the need for this assumption. Often a sufficiently high-quality beam profile is not available to users; in this case the adaptive-subtraction fitting method provides a fast way of significantly improving qualitative data. This is therefore a useful tool for retrospective analysis. It is recommended that, for future SR-XRF microscopy, users obtain a beam profile for accurate quantitative measurements.

To compare the two methods, the data acquired at ID21, where a wire scan was available, were processed using the adaptive-subtraction correction method and the results are shown in Fig. 10. The artefacts present in the original image are significantly reduced whilst maintaining low-concentration features. There are differences between the outputs of each correction method, which have several causes. A high-quality background fit in the adaptive subtraction is essential for generating an appropriate correction. Image data containing high amounts of noise and low statistical discrimination between features and background affect the adaptive subtraction more so than the beam-profile normalization. For this reason, the adaptive subtraction corrects the I18 data in Fig. 9 very well (four orders of magnitude between the background and features), whereas the ID21 data are not corrected as well (since there are only two orders of magnitude between the background and features). As mentioned previously, the beam-profile correction includes a re-normalization step and therefore the magnitude of the correction will be closer to the real value than the adaptive subtraction. However, the beam-profile correction relies on an accurate representation of the X-ray profile; errors associated with this measurement may also account for some of the differences between the two correction methods.
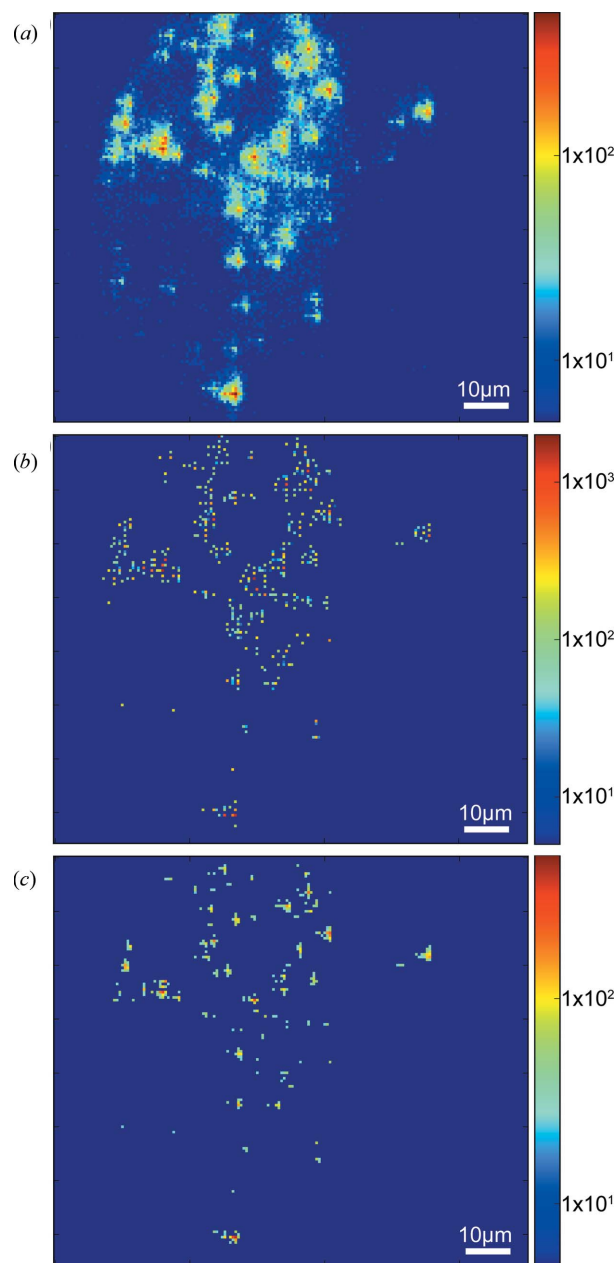

Figure 10
Ti XRF map recorded at ID21. (*a*) Original Ti XRF map. (*b*) After beam-profile correction. (*c*) After adaptive-subtraction. The coloured bar represents the number of counts, displayed on a logarithmic scale.

These corrections methods improve the accuracy of quantitative XRF microscopy by addressing the assumption of a perfectly uniform, binary, square-function beam profile. However, other complications/assumptions are still present in these systems including the assumption of a single matrix when correcting for fluorescence attenuation (Kanngiesser, 2003; Sitko & Zawisza, 2012). It is important to consider all aspects that reduce the accuracy of quantification, not solely the beam profile. A fundamental way to reduce the effects of attenuation errors is by optimizing the sample preparation by producing thin sections (Szczerbowska-Boruchowska, 2012). This limits the range of fluorescence attenuation observed

throughout the sample caused by differences in local density (Bewer, 2015).

4. Conclusions

The presence of XRF image artefacts generated by the profile of a typical synchrotron focused X-ray beam has been reported. These artefacts significantly affect qualitative and quantitative analyses and must be considered depending on the sample elemental distribution. Obtaining an accurate two-dimensional representation of the X-ray beam profile enables post-analytical corrections to the image. The beam-profile correction considers the distribution of the flux within the profile and how this affects the measured images. The process includes an intensity redistribution within the map, generating more realistic concentration distributions. An alternative adaptive-subtraction method that does not rely on a beam profile can be utilized for retrospective analysis. Both correction methods allow the entire elemental distribution to be visualized without the presence of the image artefacts and the beam-profile correction improves the accuracy of quantification. Although both analytical corrections are useful in their own right, the beam-profile correction is more accurate and should be favoured; therefore it is recommended that users should obtain an accurate beam profile for the most precise quantitative results.

References

Addison, O., Davenport, A. J., Newport, R. J., Kalra, S., Monir, M., Mosselmans, J. F. W., Proops, D. & Martin, R. A. (2012). *J. R. Soc. Interface*, **9**, 3161–3164.

Bewer, B. (2015). *Nucl. Instrum. Methods Phys. Res. B*, **347**, 1–6.

Eng, P. J., Newville, M., Rivers, M. L. & Sutton, S. R. (1998). *X-ray Microfocusing: Applications and Techniques*, pp. 145–157. International Society for Optics and Photonics.

Jensen, M. P., Aryal, B. P., Gorman-Lewis, D., Paunesku, T., Lai, B., Vogt, S. & Woloschak, G. E. (2012). *Anal. Chim. Acta*, **722**, 21–28.

Kanngiesser, B. (2003). *Spectrochim. Acta Part B At. Spectrosc.* **58**, 609–614.

Lanteri, H., Aime, C., Beaumont, H. & Gaucherel, P. (1994). *Optics in Atmospheric Propagation and Random Phenomena*, pp. 182–193. Belligham: International Society for Optics and Photonics.

Liu, W., Ice, G. E., Tischler, J. Z., Khounsary, A., Liu, C., Assoufid, L. & Macrander, A. T. (2005). *Rev. Sci. Instrum.* **76**, 113701.

Mori, Y., Yamauchi, K., Yamamura, K., Mimura, H., Sano, Y., Saito, A., Ueno, K., Endo, K., Souvorov, A. & Yabashi, M. (2002). *X-ray Mirrors, Crystals, and Multilayers II*, pp. 58–65. International Society for Optics and Photonics.

Mosselmans, J. F. W., Quinn, P. D., Dent, A. J., Cavill, S. A., Moreno, S. D., Peach, A., Leicester, P. J., Keylock, S. J., Gregory, S. R., Atkinson, K. D. & Rosell, J. R. (2009). *J. Synchrotron Rad.* **16**, 818–824.

Paunesku, T., Vogt, S., Maser, J., Lai, B. & Woloschak, G. (2006). *J. Cell. Biochem.* **99**, 1489–1502.

Rousseau, R. M. & Boivin, J. A. (1998). *Rigaku J.* **15**, 13–15.

Sage, D., Donati, L., Soulez, F., Fortun, D., Schmit, G., Seitz, A., Guiet, R., Vonesch, C. & Unser, M. (2017). *Methods*, **115**, 28–41.

Salomé, M., Cotte, M., Baker, R., Barrett, R., Benseny-Cases, N., Berruyer, G., Bugnazet, D., Castillo-Michel, H., Cornu, C., Fayard, B., Gagliardini, E., Hino, R., Morse, J., Papillon, E., Pouyet, E., Rivard, C., Solé, V. A., Susini, J. & Veronesi, G. (2013). *J. Phys. Conf. Ser.* **425**, 182004.

Shaevitz, J. W. & Fletcher, D. A. (2007). *J. Opt. Soc. Am. A*, **24**, 2622–2627.

Shaw, P. J. & Rawlins, D. J. (1991). *J. Microsc.* **163**, 151–165.

Sitko, R. & Zawisza, B. (2012). *Quantification in X-ray Fluorescence Spectrometry.* IntechOpen.

Solé, V. A., Papillon, E., Cotte, M., Walter, P. & Susini, J. (2007). *At. Spectrosc.* **62**, 63–68.

Swedlow, J. R. (2007). *Methods Cell Biol.* **81**, 447–465.

Swedlow, J. R., Sedat, J. W. & Agard, D. A. (1997). *Deconvolution of Images and Spectra*, edited by P. A. Jansson. pp. 284–309. San Diego: Academic Press.

Szczerbowska-Boruchowska, M. (2012). *X-ray Spectrom.* **41**, 328–337.

Thomsen, V. (2007). *Spectroscopy*, **22**, 46–50.

Yi, L., Liu, Z., Wang, K., Chen, M., Peng, S., Zhao, W., He, J. & Zhao, G. (2015). *Nucl. Instrum. Methods Phys. Res. A*, **775**, 12–14.

Yun, W., Lai, B., Cai, Z., Maser, J., Legnini, D., Gluskin, E., Chen, Z., Krasnoperova, A., Vladimirsky, Y., Cerrina, F., Di Fabrizio, E. & Gentili, M. (1999). *Rev. Sci. Instrum.* **70**, 2238–2241.